Water Resources Research

RESEARCH ARTICLE
10.1029/2020WR027965

Key Points:
- Wettability, surface roughness, and pore space structure have an impact on trapping efficiency
- Porous media with rough surface, as natural sands and glass-ceramic micromodels, were studied
- Wettability-controlled crossover from snap-off to by-pass trapping and spontaneous precursor thick-film flow were observed

Supporting Information:
- Movie S1
- Movie S2
- Movie S3
- Movie S4

Correspondence to:
H. Geistlinger,
helmut.geistlinger@ufz.de

Citation:
Zulfiqar, B., Vogel, H., Ding, Y., Golmohammadi, S., Küchler, M., Reuter, D., & Geistlinger, H. (2020). The impact of wettability and surface roughness on fluid displacement and capillary trapping in 2-D and 3-D porous media: 2. Combined effect of wettability, surface roughness, and pore space structure on trapping efficiency in sand packs and micromodels. *Water Resources Research*, *56*, e2020WR027965. https://doi.org/10.1029/2020WR027965

Received 24 MAY 2020
Accepted 10 JUL 2020
Accepted article online 23 JUL 2020

The Impact of Wettability and Surface Roughness on Fluid Displacement and Capillary Trapping in 2-D and 3-D Porous Media: 2. Combined Effect of Wettability, Surface Roughness, and Pore Space Structure on Trapping Efficiency in Sand Packs and Micromodels

Bilal Zulfiqar[1], Hannes Vogel[2], Yi Ding[1], Saeed Golmohammadi[1], Matthias Küchler[3], Danny Reuter[4], and Helmut Geistlinger[1]

[1]Helmholtz Centre for Environmental Research-UFZ, Halle (Saale), Germany, [2]Arcadis Germany GmbH, Darmstadt, Germany, [3]Fraunhofer ENAS, Chemnitz, Germany, [4]Chemnitz University of Technology, Chemnitz, Germany

Abstract A comprehensive understanding of the combined effects of surface roughness and wettability on the dynamics of the trapping process is lacking. This can be primarily attributed to the contradictory experimental and numerical results regarding the impact of wettability on the capillary trapping efficiency. The discrepancy is presumably caused by the *surface roughness* of the *inner pore-solid interface*. Herein, we present a comparative μ-CT study of the *static* fluid-fluid pattern in porous media with *smooth* (glass beads) and *rough* surfaces (natural sands). For the first time, a global optimization method was applied to map the characteristic *geometrical* and *morphological* properties of natural sands to 2-D micromodels that exhibit different degrees of surface roughness. A realistic wetting model that describes the apparent contact angle of the rough surface as a function surface morphology and the intrinsic contact angle was also proposed. The *dynamics* of the trapping processes were studied via visualization micromodel experiments. Our results revealed that sand and glass beads displayed *opposite* trends in terms of the contact angle dependence between 5° and 115°. *Sand* depicted a *nonmonotonous* functional contact angle dependency, that is, a transition from maximal trapping to no trapping, followed by an increase to medium trapping. In contrast, *glass beads* showed a sharp transition from no trapping to maximal trapping. Since both porous media exhibit similar morphological properties (similar Minkowski functions: porosity, surface density, mean curvature density, Euler number density), we deduce that this difference in behavior is caused by the difference in surface roughness that allows *complete wetting* and hence precursor thick-film flow for natural sands. Experimental results on micromodels verified this hypothesis.

1. Introduction

The *morphology* and *connectivity* of pore space and the *wettability* and *roughness* of the pore-solid interface determine (i) the fluid pattern formation during multiphase flow, (ii) the geometry of the displacement front, and (iii) the capillary trapping efficiency of the defending fluid by the invading fluid.

Recent research has focused on capillary trapping and the impact of *wettability* on fluid pattern formation. Wang et al. (2019) studied the combined effect of viscous and capillary forces, local disorder, and wettability using Lattice-Boltzmann simulations. The 2-D triangular stochastic lattice consisted of circular grains with a uniformly distributed grain diameter. The authors found that the trapping efficiency increased with the local disorder, whereas a reduced trapping of the defending fluid occurred when then capillary number was increased. Moreover, the authors found an interesting wetting transition from no trapping to trapping with increasing contact angle for low disorder and small capillary numbers ($\approx 10^{-5}$). This *dynamical phase transition* associated with *changes in local growth modes at the displacement front* was first discussed by Cieplak and Robbins (1988). For small contact angles ($<\theta_c \approx 90°$, i.e., water-wet rocks) cooperative filling results in a strong smoothing effect of the displacement front. For large θ (i.e., oil-wet rocks), the displacement front becomes fractal. Intuitively, one would expect the invasion front to become increasingly compact with decreasing θ. However, depending on the *morphology* and *connectivity* of the pore space, a second wetting

transition from compact duct flow to fractal corner flow is possible. Hu et al. (2017, 2018; silica micromodels) and Zhao et al. (2016; polymer-based micromodels) observed this second wetting transition in 2-D micromodels at a critical θ_c of 45°. Both micromodels exhibited a *smooth* pore-solid interface and rectangular pore walls, that is, the grains are cylinders. For such a rectangular pore wall geometry, corner flow occurs at a θ of 45°. A question remains regarding whether this transition can be observed in 3-D porous media with smooth surfaces (e.g., glass beads) (see Part 1 of the study; Geistlinger & Zulfiqar, 2020), or in 2-D micromodels with different *pore space structure* and *connectivity*.

AlRatrout et al. (2018) proved that surface roughness and wettability are correlated at least at the pore scale using μ-CT. Surface roughness leads to a wide distribution of the *apparent* contact angle for the mixed-wet state. Phenomenologically, this can be described by Wenzel's model (also denoted as *Wenzel's argument*; Blunt, 2017; Wenzel, 1936), where the *apparent* contact angle, $\theta^* = \arccos(r \times \cos(\theta_0))$, is a function of surface roughness (r) (i.e., the ratio of the surface area to the flat surface area) and the intrinsic contact angle (θ_0) (i.e., the contact angle on a flat surface). A rough surface with varying degrees of r causes a distribution of apparent contact angles and magnifies the underlying wetting properties. For the mixed-wet state ($\theta_0 \approx 90°$), the apparent contact angle deviates in both directions and thus causes a wide θ^*distribution.

This simple model was criticized by de Gennes (1985) because small values of r ($\approx$1.1) caused *complete* wetting ($\theta^* = 0$) on rough glass surfaces ($\theta_0 \approx 20°$). However, this was not observed experimentally (Bico et al., 2001; Shibuichi et al., 1996). A more realistic wetting model has to include the morphology of the rough surface, for example, that the penetrating wetting film only wets the "valleys" of the rough surface. In the present paper, a realistic wetting model is proposed that describes the apparent contact angle as a function of the dry and wet parts of the rough surface as well as the intrinsic contact angle. Even though *complete wetting* is supposed to occur on rough silica surfaces (AlRatrout et al., 2018; Blunt, 2017; Wang et al., 2020), experimental proof is still lacking.

It is questionable if μ-CT with a resolution of 2 μm (AlRatrout et al., 2018) can resolve the surface roughness of natural sand of a few micrometers in diameter (Kibbey, 2013). Furthermore, the μ-CT study only analyzed the *static* fluid-fluid distribution. Therefore, an understanding of the combined effect of surface roughness and wettability on the *dynamics* of the trapping process is currently lacking.

Representative 2-D micromodels with varying degrees of surface roughness could be an alternative for studying the process dynamics. These micromodels must represent the characteristic *geometrical* and *morphological* properties of the 3-D porous medium.

The only recent publication that reported on a study of the impact of surface roughness on the fluid-fluid displacement process (i.e., air displaces the wetting fluid oil; $\theta_0 \cong 20°$ and $\mu_{oil} = 0.15$ Pa s) within 2-D-glass micromodels is that of Mehmani et al. (2019). The pore network in this study consisted of a regular quadratic lattice of circular grains (grain diameter = 270 μm, grain height = pore depth = 10–20 μm, and porosity $\cong$ 0.5). We note that a *regular* (not stochastic) lattice was used to represent a 3-D porous medium (sandstone). The roughness was introduced by placing a cream etchant on the glass substrate prior to thermal bonding. Roughness was measured by the averaged hillock-height-to-pore-depth ratio (Ω). The drainage experiments were conducted for different degrees of surface roughness (Ω (%) = 0, 0.2, 6.0, 13.0) at unrealistically small capillary numbers ($\approx 10^{-8}$). The authors observed an increased sweep efficiency of 14% when roughness was increased from 6% to 13%. However, the authors could not quantitatively differentiate the finger morphology and topology on the basis of surface roughness. Perimeter-to-area ratio values and Euler numbers showed negligible differences among the finger paths within the different micromodels. Accordingly, we hypothesize that a higher sweep efficiency is caused by the denser pore network because the addition of hillocks between the regular grains creates a stochastic lattice of hillocks and cylindrical grains. The classical phase diagram of Lenormand et al. (1988) gives at Log (μ_{air}/μ_{oil}) ≈ -4 and Log (Ca) ≈ -8 viscous fingering (see Figure 4a in Lenormand et al., 1988).

The micromodels used in previous studies were thus neither representative of the pore space morphology, grain geometry, or surface roughness of natural sands (Kibbey, 2013). In current literature, there is limited information on 2-D sand analogs (i.e., representative micromodels) with different degrees of surface roughness.

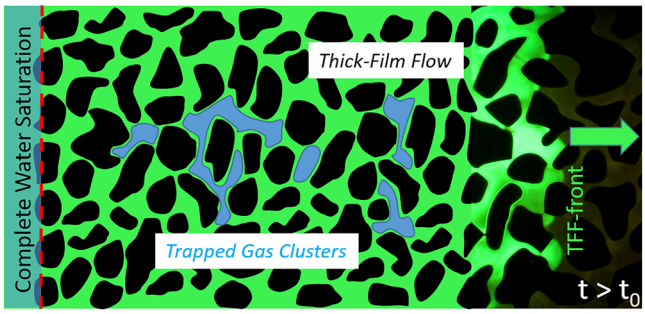

Figure 1. Schematic: Spontaneous precursor TFF (green area) and water redistribution over the rough pore-solid interface of the entire pore network (glass ceramic micromodel) at time $t > t_0$. Water was injected into the micromodel on the left side and injection was stopped at t_0. Water is drawn from the complete saturated region (red dashed line). The interplay of precursor TFF and CF leads to snap-off trapping of the defending fluid (blue clusters) in front of the water-saturated region.

As an instructive example we discuss the dynamics of the trapping process in a water-wet system (siliceous porous media with a rough surface, such as natural sand or glass ceramic micromodels; intrinsic contact angle $\theta_0 \approx 20°$). The different capillary flows are governed by the order of driving capillary pressures. First, a precursor thick-film flow (TFF) will "spontaneously" invade the porous media assuming that surface roughness leads to *complete* wetting of the rough surface. This causes a *continuous* TFF throughout the *entire* porous media and a *redistribution* of the water phase. Figure 1 shows a spontaneous invasion experiment. In this range of capillary numbers, both the invading and the defending fluids can be continuous in 2-D porous media (micromodels); that is, TFF allows bicontinuity of both phases, which is only possible for duct flow (DF) in 3-D porous media (Adler & Brenner, 1988).

When the capillary number is increased up to 10^{-6}, CF occurs and capillary trapping is controlled by the interplay of TFF and CF in front of the main DF-displacement front (blue clusters in Figure 1). This interplay leads to very efficient trapping mechanisms in rough, water-wet porous media. The *continuous* TFF (*complete* wetting) can reach any region of the pore space and "feed" CF. This *swelling* of the corner water phase can lead to *unstable* fluid-fluid interfaces depending on the pore-channel geometry. The unstable interface will "jump" across the whole duct cross section and form a more stable interface, that is, a full duct meniscus. This is the basic mechanism of snap-off trapping.

We emphasize that this efficient snap-off trapping mechanism needs two necessary requirements: (i) spontaneous continuous TFF (complete wetting on rough surfaces) and (ii) CF that can lead to unstable fluid-fluid-interface configurations (an irregular geometrical shape of the throats or grains). In short, we denote the first requirement as the *complete wetting* condition, and the second requirement as the *geometrical instability* or *snap-off* condition.

In Geistlinger and Zulfiqar (2020), we studied the impact of wettability on fluid pattern formation and capillary trapping in 3-D glass bead packs during fluid invasion at a capillary number of 10^{-7} using μ-CT. The invading fluid was water and the defending fluid was air. The contact angle of the glass beads was altered between 5° and 115° using Piranha cleaning and salinization. We found a sharp transition in the trapping efficiency at a contact angle of ≈90°. The key question is whether this interesting dynamical phase transition will occur in (i) sediments with rough surfaces (e.g., sand or sandstones), and (ii) sediments with more irregularly shaped grains compared to spherical glass beads. Therefore, part two of our current study focuses on natural sands and micromodels with a rough pore-solid interface. The first objective is to investigate the trapping efficiency in natural sands by changing the contact angle between 5° and 115° using μ-CT and to then analyze the static fluid-fluid pattern. The second objective is to visualize the trapping dynamics using representative 2-D micromodels (2-D sand analogs) with different pore space structures and different surface roughness values to test the complete wetting and the geometrical instability condition using high-resolution optics and fluorescence microscopy.

2. Material and Methods

2.1. Sands and Fluids

Natural sand (NS, filtered and fine quartz sand, *mgsdekorations*, Germany) with a sieve fraction of 0.75–1.25 mm and an average diameter of 1.04 ± 0.07 mm was used for this study. Close random packing (Dullien, 1992) was achieved for all experiments with a packing density of 1,572 kg/m^3 and a porosity of 0.39. Water ($\rho_w = 998$ kg/m^3, $\mu_w = 1.002 \times 10^{-3}$ Pa s, $\sigma_{gw} = 72.86 \times 10^{-3}$ N/m) and air ($\rho_g = 1.184$ kg/m^3, $\mu_g = 1.84 \times 10^{-5}$ Pa s) were used as the invading and defending fluids, respectively.

2.2. Experiments

The experimental procedure for wettability alteration, experimental setup, and methodology follows the same protocols described in Part 1 (Geistlinger & Zulfiqar, 2020). We studied NS with different wettability:

Table 1
Contact Angle (θ) Dependence of the Residual Gas Saturation $S_{g,res}$ in % for Six Fluid Invasion Experiments (Invading Fluid: Water; Defending Fluid: Gas)

Replicate Experiment	θ (°)	1 $S_{g,res}$	2 $S_{g,res}$	3 $S_{g,res}$	4 $S_{g,res}$	$S_{g,res}$-mean
NS1	5	12.46	13.60	12.73	13.20	13.00 ± 0.50
NS2	33	11.55	10.90	11.72	11.32	11.37 ± 0.35
NS3	81	0.80	0.20	0.10	0.35	0.36 ± 0.31
NS4	88	1.71	1.54	1.32	1.27	1.46 ± 0.20
NS5	99	6.32	6.65	5.90	6.08	6.24 ± 0.32
NS6	115	6.86	6.98	6.56	6.10	6.62 ± 0.39

Note. Each experiment was repeated four times (replicates 1–4).

NS1: *strongly water wet* ($\theta = 5°$), NS2: *weakly water wet* ($\theta = 33°$), NS3–5: *intermediate wet* ($\theta = 81°, 88°, 99°$), and NS6: *weakly air wet* ($\theta = 115°$).

For the fluid invasion experiment, a Plexiglas column of 200 mm length and 19.1 mm inner diameter was packed with the NS. For all experiments, close random packing with approximately identical pore size distribution (PSD, 0.290 ± 0.12 mm) was achieved. The PSD was derived by the first Minkowski function of the pore space (Geistlinger et al., 2015). To avoid grain rearrangement during fluid invasion, lead spheres (diameter = 3.1 mm and density = 11.35×10^3 kg/m^3) were placed for a height of 30 mm on top of the NS. The six different experiments are denoted according to their increasing contact angle (NS1 to NS6).

A series of 24 fluid invasion experiments were conducted (four replicates for each specific NS-type, Table 1). Air-saturated water was injected with a volumetric flow rate $q_w = 0.82$ mm^3/s with a front velocity of 0.007 mm/s, corresponding to a capillary number of 10^{-7}. The air-saturated water was injected using a high-precision bidirectional syringe pump with a step resolution of 0.046 μm (Fusion 200, Chemyx, Stanford, USA).

2.3. Computed Microtomography and Image Processing

The fluid-fluid pattern and the pore space structure were recorded after each injection experiment, and analyzed at three different sections of the column using computed X-ray microtomography. An Industrial X-ray scanner with a focal spot of 3 μm was used (X-Tek XTH 225, Nikon Metrology, Belgium). The projections were recorded on a Digital Perkin Elmer 1620 Flat Panel Detector with a resolution of 2,000 × 2,000 pixels. To maneuver full range of gray values, optimum energy settings (155 μA, 120 kV, 18.6 W) were used and beam-hardening artifacts were reduced by using a 0.1 mm copper filter.

The spatial resolution of the CT image (0.013 mm) is important, as it determines the threshold at which a fluid meniscus in a pore throat can be detected. For close random packing, the mean pore-throat diameter can be estimated by $d_{k,min} = 0.31 \times 0.92$ mm = 0.29 mm (=minimal pore diameter, Geistlinger et al., 2006). Hence, the fluid meniscus can be reasonably resolved by 22 voxels along the diameter. Image processing was carried out according to the protocol described in Part 1 of the study (Geistlinger & Zulfiqar, 2020).

2.4. Micromodel Experiments

2.4.1. Microstructures

Experiments were conducted using two different stochastic pore space structures, which exhibit different morphology and connectivity of the pore space and different geometrically shaped grains and pore channels. Figures 2a) and 2b) show sections of the irregular pore space structure (MM4 micromodel) and of the regular pore space structure (MM5 micromodel), respectively. The dimensions of the micromodels were 80 mm × 80 mm × 0.3 mm.

Irregular pore space structure/micromodel MM4 (Figure 2a): A 3-D-2-D-mapping algorithm was developed to map certain statistical properties of 3-D to 2-D porous media. The horizontal and vertical *chord length distribution* (CLD) of *grains* and *pores* were used as mapping constraints. The chord length distributions are sensitive measures (i) of the pore space morphology and topology and (ii) of the grain geometry (Brücher & Bottlinger, 2006). Strong connected pore systems possess a high fraction of long chords, whereas dense pore systems possess a high fraction of short chords. A high peak in the grain-CLD shows that the particle size distribution is narrow. A second weak peak in the grain-CLD indicates contact points between neighboring grains. Nonspherical grains show an asymmetry between horizontal and vertical chords. The CLDs of a 1 mm sand (details in Geistlinger et al., 2015) were used for the 3-D-2-D mapping, so that the irregular MM4 microstructure has similar morphological, topological, and geometrical properties. The global optimization method *Simulated Annealing* (Schlueter et al., 2010) starts with a randomly generated pixel distribution that has the average porosity of the 3-D structure (=0.39) and changes the pixel configuration until the 2-D structure has the specified properties of the 3-D structure, that is, the same CLDs.

Regular pore structure/micromodel MM5 (Figure 2b): The square lattice microstructure contains 80 × 80 equidistant sites connected by lognormal distributed throats (Matlab-generator with a throat width

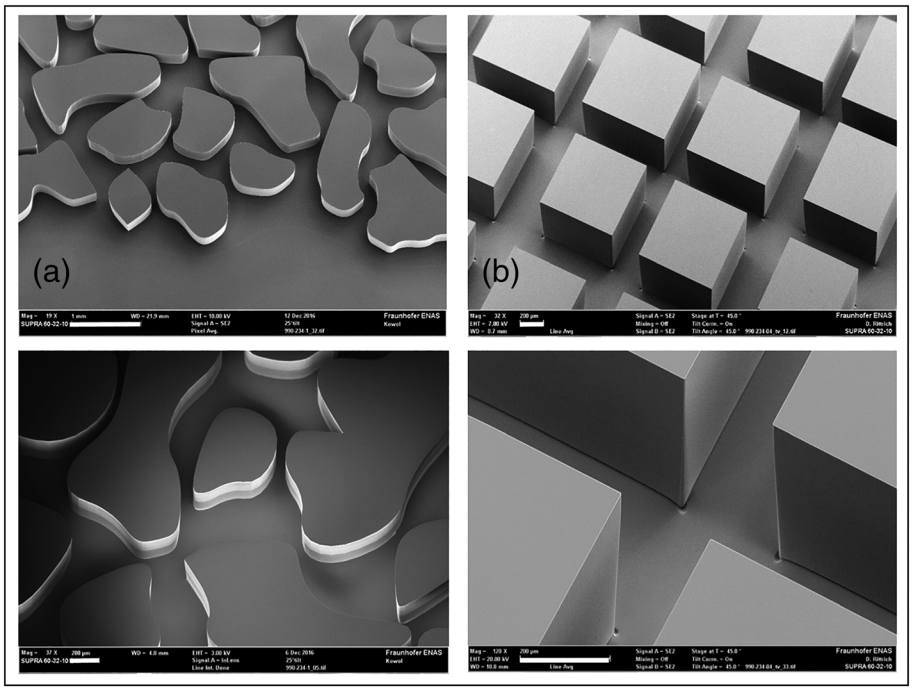

Figure 2. SEM images of the silicon micromodels with (a) irregular (MM4) and (b) regular (MM5) stochastic pore space structure. The white resolution bars correspond to 1 mm (left top) and to 200 μm in all other figures.

$d_{throat} = 400 \pm 62$ μm). We note that this microstructure is similar to that used by Lenormand et al. (1988) for deriving their famous phase diagram on fluid pattern formation. Their chemical etched square-lattice microstructure consists of rectangular throats (ducts), which have a log-normal distributed width and a constant etching depth of 1 mm. A discrete frequency distribution was used with seven size classes from 100–600 μm. The mean throat width of 350 μm corresponds to the throat width of 400 μm of the regular MM5 microstructure.

2.4.2. Production of Silicon Micromodels

A microfabrication method involving photolithography, inductively coupled plasma-deep reactive ion etching (ICP-DRIE) and anodic bonding was used to fabricate the micromodel in a silicon wafer. An interval-based ICP-DRIE technology (Kuechler et al., 2003; Zue et al., 2013) was applied for anisotropic etching. This resulted in high edge steepness and a true mapping of the lattice structure with depth (Figure 2b), that is, only minimal underetching is produced (1.2° deviation from the vertical line, and maximal deviation from the horizontal bottom line of 10 μm). This 1.2° deviation was achieved for a ninefold deeper microstructure compared to the microstructure produced by Zue et al. (2013). The production process is described in Geistlinger et al. (2019) to which the reader is referred for additional details.

2.4.3. Production of Glass Ceramic Micromodels

The 2-D micromodel was constructed by using a photolithographic etching process (Invenios Europe GmbH). As solid material, a photosensitive glass ceramic FOTURAN (Schott-GmbH) was used. The chemical etched microstructure was covered with a plain glass plate by thermal-diffusion bonding (500°C), and hydraulic tube connections were installed at the inlet and outlet triangle. After complete construction, the etched structures were cleaned by isopropanol flushing, subsequent water flushing and final drying at 200°C.

The SEM images of the MM5 micromodel (Figure 3) show the microstructure at different magnifications indicating the high accuracy of the *anisotropic* photolithographic etching process compared to *isotropic* chemical etching (underetching) of glass micromodels. Considering the sharpness/slope of the grain wall, this accuracy is in the order of 10 μm. The main feature of the microstructure is the surface roughness, which is caused by the glass ceramic. The mean roughness was determined by the grain size distribution of the sintered glass powder which is 1–3 μm as provided by the producer (Invenios Europe GmbH) (see Figure 3b). The estimated surface roughness parameters (ISO-standard, 1997; Voburger & Raja, 1990) are

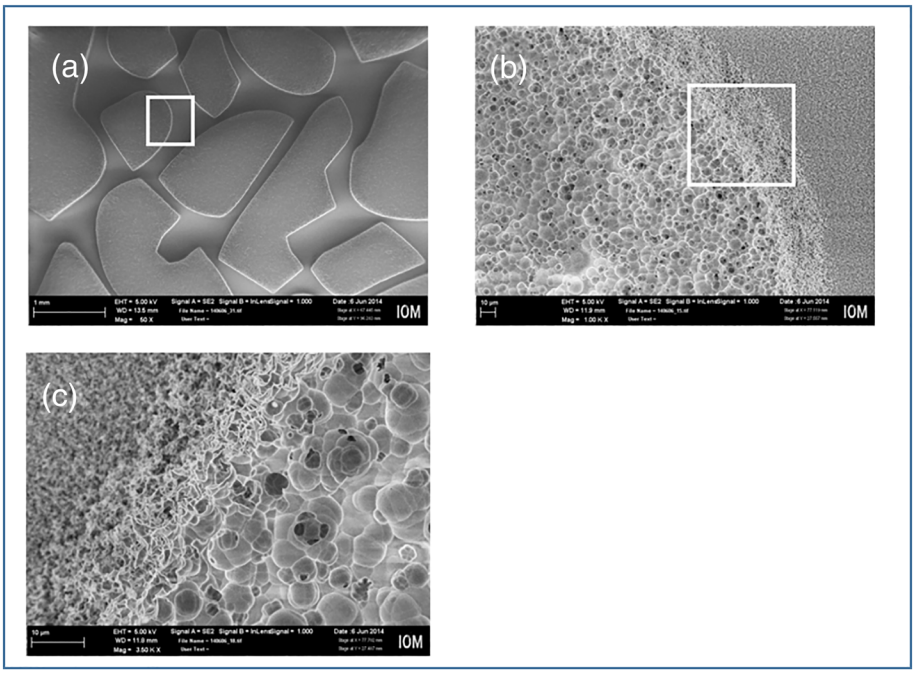

Figure 3. SEM images of the *rough pore-solid interface* of glass ceramic micromodels (irregular MM4 microstructure) at different magnifications: (a) Scale bar = 1 mm; (b) grain boundary indicated by the white rectangle in Figure 3a; scale bar = 100 μm, (c) grain boundary at higher magnification; white rectangle in Figure 3b, scale bar = 10 μm.

the mean surface height R_a ($\equiv \delta = 1$ μm) and the wavelength parameter D ($\equiv \lambda = 2$ μm) indicating the periodicity of the surface (Geistlinger et al., 2015).

2.4.4. Experimental Setup and Visualization

To perform imbibition experiments at a constant flow rate ($Ca = 10^{-7}$ to 5×10^{-5}), a high-precision bidirectional syringe pump with a step resolution of 0.046 microns (Fusion 200, Chemyx, Stanford, USA) was used. As the wetting fluid, water was used, and air was used as the nonwetting fluid.

For visualization, we used an SLR-camera Canon EOS7D with a 100-mm Macro lens (Canon EF 100-mm F2.8 USM Macro lens) both in the single-shot mode (spatial resolution: 5,184 × 3,456 pixel) and in the video mode with 24 frames/s (spatial resolution: 1,920 × 1,080 pixel). Furthermore, a fluorescence microscope in combination with the SLR-camera was used (Leica Leitz DMRB microscope; LM digital SLR wide-field adapter, micro-tech-lab Ltd.). Uranin was used as a fluorescent tracer.

3. Experimental Results: Trapped Gas Saturation and Cluster Shape

Figure 4 compares the contact angle dependency of the trapped gas saturation for sands and glass beads. When the contact angle is increased sand and glass beads displayed *opposite* trends in terms of the contact angle dependence: *Sand* shows a *nonmonotonous* functional contact angle dependency, that is, a transition from maximal trapping (residual gas saturation $S_{g,res} \cong 13\%$) to no trapping and then an increase to medium trapping ($S_{g,res} \cong 7\%$). *Glass beads* show a *monotonous* behavior, that is, a sharp transition from no trapping to maximal trapping ($S_{g,res} \cong 7\%$).

Since both porous media exhibit similar morphological properties (similar Minkowski functions: porosity, surface density, mean curvature density, Euler number density), we deduce that this difference in behavior is caused by the difference in surface roughness that allows *complete wetting* and hence precursor thick-film flow. This causes a highly efficient snap-off trapping mechanism, which yields a maximal residual gas saturation of approximately 13% (experiment NS1, Table 1). Increasing the contact angle up to 33° the residual gas saturation is still high and about 11% (Table 1).

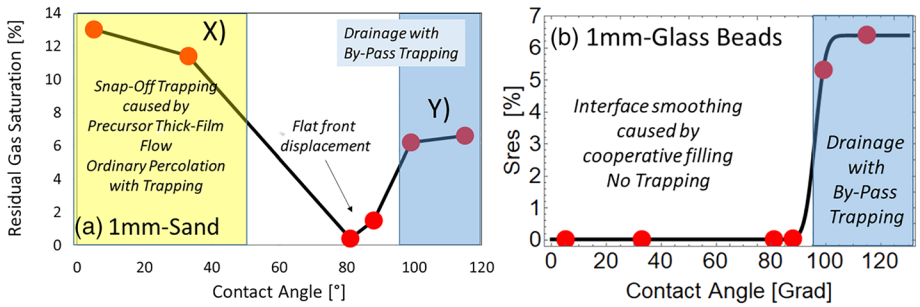

Figure 4. Contact angle dependency of the trapping efficiency for (a) 1 mm sand, and for (b) 1 mm glass beads (Geistlinger & Zulfiqar, 2020). (a) The yellow marked area shows the region of snap-off trapping caused by precursor TFF. The spatial cluster distribution X of snap-off trapping is shown in Figure 5x. The blue area is the region of drainage with bypass trapping. Its trapped cluster distribution Y is shown in Figure 5y. (b) Sharp transition of trapping efficiency at $\theta_c = 96°$. White area: Interface smoothing hinders gas trapping. Blue area: Region of drainage-like displacement with bypass trapping. Note the different scales of the y axes. Left: $y_{max} = 14\%$, right: 7%.

We think that the reason for this small decrease is the heterogeneous wettability of NS caused by its nonhomogeneous surface roughness, that is, some parts of the surface are smooth while other parts are rough (see Figure 1 in Kibbey, 2013). Therefore, the degree of surface roughness r is smaller compared to that of micromodels produced by glass ceramic and, consequently, Wenzel's argument will lead to a smaller range of contact angles, where complete wetting is possible.

The shape of the trapped gas clusters and their spatial distribution are shown in Figure 5x. Because the clusters are trapped within the *macropores*, they are extended over many pores and their shape is ganglia-like. The cluster size distribution of 1 mm sand packs (Figure 5x) shows *universal scaling* behavior. This supports the *dynamical trapping model* for low flow rates (Lenormand & Zarcone, 1984; in the following denoted as L&Z84), namely that the trapping mechanisms can be described by *Ordinary Percolation* with trapping (Wilkinson, 1984). The cluster shape and size analysis of the trapped gas clusters within glass ceramic micromodels and packs of natural sand will be published elsewhere.

Based on Wenzel's argument one expects a transition in trapping efficiency with an increase in contact angle to some critical value around 90°. Indeed at $\theta = 81°$ (experiment NS3) no gas is trapped. This is a strong indicator that the *complete wetting* and hence *precursor TFF* is not possible. Therefore, the highly efficient snap-off trapping mechanism is suppressed for contact angles larger than 81°. In the range of *neutral* contact angles (≈90°; NS3 and NS4) capillary forces are nonexistent, which leads to flat menisci and to a flat front advance. Therefore, capillary bypass trapping is not possible.

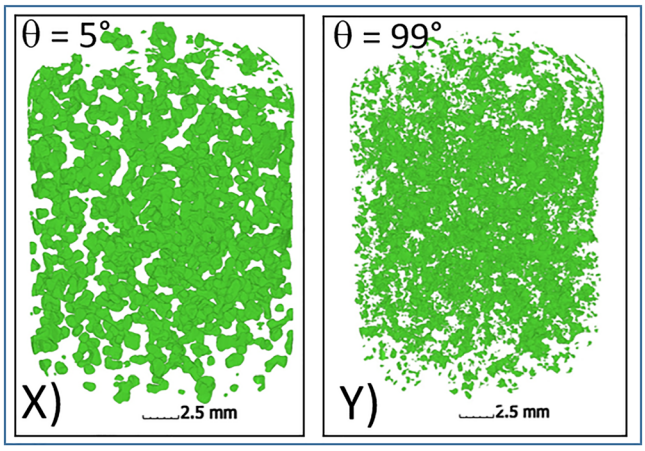

Figure 5. Spatial cluster distribution in 1 mm sand packs for different contact angles: (x) 5° and (y) 99°; compare with Figure 4a.

Increasing the contact angle up to 99° (NS5) and 115° (NS6), the sand becomes hydrophobic and the invading fluid water is now the nonwetting fluid. The character of the displacement process changes from imbibition to drainage. Therefore, the displacement process for NS5 and NS6 can be understood as a drainage process with bypass trapping. This leads to a residual gas saturation of 6.6%, that is, the trapping efficiency for high contact angles is approximately half of the trapping efficiency for small contact angles. Inspecting the shape of the trapped gas clusters and their spatial distribution shown in Figure 5y, one recognizes that gas as the wetting fluid is now trapped within the small pores (see the occupational frequency of small pores, Figure 9 in Geistlinger & Zulfiqar, 2020).

It is instructive to compare the normalized trapped gas phase for 2-D sand analogs (micromodels MM4 glass ceramic, MM4-Si) and 3-D porous media (sand packs and GBS packs) shown in Figure 4. $S_{g,\,max}^{MM4-glass}$ (=73%) is used as a normalization factor for the micromodels (red symbols) and $S_{g,\,max}^{sand}$ (≅13%) is used for 3-D porous media (sand: blue rhombs, GBS: gray circles).

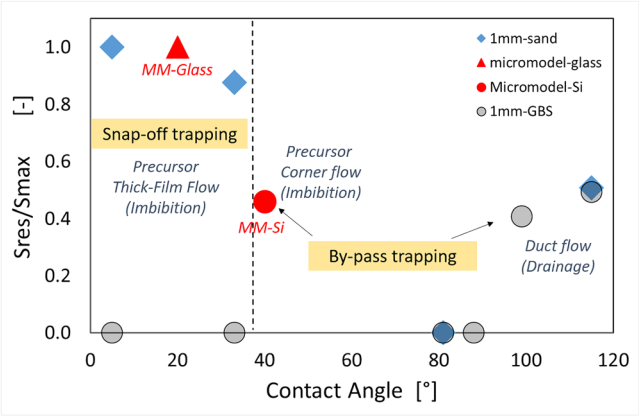

Figure 6. Comparison of trapping efficiency (= normalized residual gas saturation = $S_{g,res}/S_{g,max}$) in 2-D sand analogs (micromodels MM4 glass ceramic, MM4-Si) and 3-D porous media (1 mm sand packs, 1 mm GBS packs). Note that different normalization factors $S_{g,max}$ are used, which are given in the text.

The main conclusion from Figure 6 is that the transition from snap-off trapping to bypass trapping causes a reduction of trapping efficiency of about 50% in all cases. Interesting is that the drainage process at high contact angles ($\theta = 115°$) leads to bypass trapping with nearly the same trapping efficiency $S_{g,res} \cong 7\%$ (the symbols for sand and glass beads—blue rhomb and gray circle - cover each other).

4. Discussion: Physical Mechanisms and Micromodel Experiments

In this section we will discuss physical mechanisms and constraints, which control the *trapping dynamics* using visualization micromodel experiments. We will test these trapping constraints (conditions) using micromodels with different pore space structure and surface roughness. We will show that the interplay of geometrical and surface properties of the pore space lead to different capillary trapping mechanisms. We emphasize that one has to distinguish CF bypass trapping from standard DF bypass trapping. The discussion in the previous section was based on the *hypothesis* that *complete wetting* on rough silica surfaces can occurs for an intrinsic contact angle of ≈20°. For the first time we will provide experimental evidence for the *complete wetting* hypothesis.

4.1. Physical Mechanisms

4.1.1. Complete Wetting Condition: Impact of Precursor Thick-Film Flow on Capillary Trapping

The wetting behavior of an ideal flat solid is fixed by its chemical composition and local or intrinsic contact angle θ_0 (Young's relation). But real solids are rough, which affects their wettability (Bico et al., 2001; Cazabat & Stuart, 1986; Johnson & Dettre, 1964; Netz & Andelman, 1997). Figure 7 shows a rough surface in contact with a water reservoir and a water film propagating along the rough surface. The Young relation is locally valid and for *partial wetting* the water flow stops and a certain section of the rough surface remains dry. At this position the *Free Energy F* of the three-phase system "water-air-solid" has reached its minimum (thermodynamical equilibrium: $dF = 0$).

A *spontaneous TFF* occurs (blue arrow in Figure 7) if its *Free Energy* can be lowered by moving forward, that is, if the corresponding increment dF is negative for a given θ_0. In this case the TFF will further advance and cover the entire rough surface, that is, *complete wet* the rough surface.

Let us considers a water film of length L_{LV} (the length of the flat gas-water contact line; Figure 7) that covers a rough siliceous surface with a contact line L_{SL}, then the change in *Free Energy* in the x direction is given by

$$dF = (\gamma_{SL} - \gamma_{SV})(r - \phi_S)dx + \gamma_{LV}(1 - \phi_S)dx = \quad (1a)$$

$$= (\gamma_{SL} + \gamma_{LV} - \gamma_{SV})(1 - \phi_S)dx + (\gamma_{SL} - \gamma_{SV})\Delta r dx, \quad (1b)$$

where γ denotes the free energy per area of the solid/vapor (S/V), solid/liquid (S/L), and liquid/vapor (L/V) interface, also known as the surface tension, ϕ_S denotes the solid fraction that remains dry (i.e.,

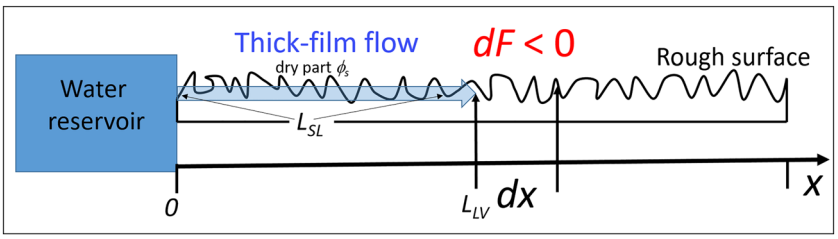

Figure 7. Thermodynamical *complete wetting* condition for *spontaneous* thick-film flow (blue arrow) on a rough surface (length L_{SL}): A small film advance from $x = L_{LV} + dx$ leads to a negative increment of the *Free Energy* (dF < 0). The thick film penetrates the rough surface and wets the "valleys" completely and leaves the "hills" dry. The dry part of the rough surface is denoted by ϕ_s (Bico et al., 2001; de Gennes, 1985).

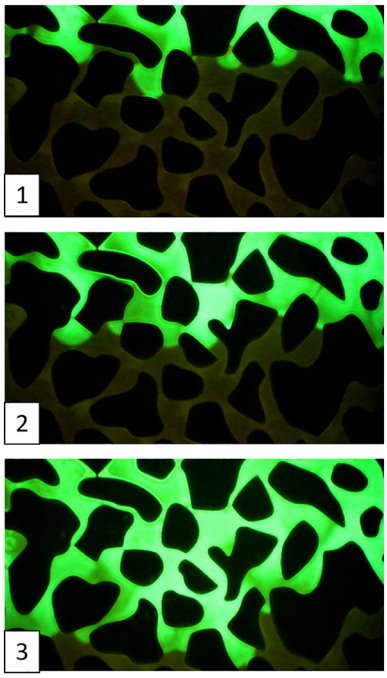

Figure 8. Precursor TFF in rough MM4-glass ceramic micromodels (2-D sand analog) at very low capillary number $<10^{-6}$. The images from top to bottom show the displacement front at subsequent times (Uranin tracer, fluorescence microscopy).

the fraction of the solid surface that is not wetted within the water film area) and r denotes the solid roughness ($= L_{SL}/L_{LV}$, $\Delta r = (L_{SL} - L_{LV})/L_{LV}$).

In the case of oxidic solid surfaces, the *Free Energy* ($\gamma_{SL} + \gamma_{LV}$) is always smaller than γ_{SV} (de Gennes, 1985). Therefore, the system lowers its *Free Energy* if wetting proceeds ($dx > 0$; first term in Equation 1b = flat surface term). The wetting behavior is enhanced on rough surfaces because the roughness term (second term in Equation 1b) leads also to a decrease in *Free Energy* if wetting proceeds. Hence, roughness magnifies hydrophilic wetting behavior (Wenzel's argument). Searching for the minimum of F and using Young's equation ($\gamma_{LV}\cos(\theta) = \gamma_{SV} - \gamma_{SL}$), the critical contact angle ($dF = 0$) follows from Equation 1a and the *complete wetting* condition is given by

$$\theta_0 < \theta_c, \quad \text{with } \theta_c = \arccos\left(\frac{1-\tilde{\phi}_s}{r-\phi_s}\right), \tag{2}$$

where θ_0 is the equilibrium contact angle of the liquid on an ideal flat surface of the same chemical composition (= intrinsic contact angle) and $\left(1-\tilde{\phi}_s\right)\cdot L_{LV}$ is the surface area of the flat water film (Bico et al., 2001). The physical meaning of Equation 2 is that for all $\theta_0 < \theta_c$, the increment dF of the *Free Energy* is negative (shown in Figure 7). This forces the TFF to advance as long as the entire surface is covered by a water film. The range of the critical contact angle is determined by the degree of surface roughness r. For a flat surface ($r = 1$), complete wetting and hence spontaneous TFF is only possible for $\theta_0 = 0$. For large values of $r \gg 1$ and this is the typical case, the critical contact angle is $\pi/2$. Consequently, *complete wetting* of rough surfaces is possible for a broad range of intrinsic contact angles: $\theta_0 < \pi/2$. Equation 2 yields for the rough surface of the glass ceramic micromodels (roughness parameter: $\delta = 1\,\mu m$, $\lambda = 2\,\mu m$) a critical contact angle of 57°, where a hemisphere geometry was assumed, that is, an array of sintered spherical powder grains. The radius of a single hemisphere was estimated by λ and the thickness of the penetrating water film by $\delta/2$. Consequently, one expects complete wetting for the glass ceramic micromodels ($\theta_0 \approx 20°$).

Figure 8 shows spontaneous TFF advance at three subsequent times and at very low capillary numbers ($<10^{-6}$) after water injection was stopped. The TFF redistributes the water of the saturated region (region left from the red dashed line shown in Figure 1) over the *whole* rough surface of the micromodel. This interesting wetting behavior of *continuous* capillary flow at *no* water injection, that is, complete wetting of a rough silica surface, is shown in a video provided in the supporting information (Movie S1-MM4-glass ceramic-TFF). The experimental observation of spontaneous capillary flow at *no* water injection verifies the *complete wetting hypothesis*.

4.1.2. Geometrical Instability Condition

Besides the wetting properties, capillary trapping is also controlled by the pore space geometry. In order to understand the geometrical constraints one has to consider the capillary pressures for certain meniscus configurations. Following L&Z84 the capillary pressure for piston-like displacement (duct flow) in a quadratic duct with width a (Figure 9a; curvature of the whole meniscus) is given by

$$p_{c,\,p} = 4\sigma\cdot\frac{\cos(\theta)}{a} \quad \overset{\theta=0}{\Longrightarrow} \quad \frac{4}{a}\,\sigma. \tag{3a}$$

The snap-off capillary pressure is

$$p_{c,\,so} = 2\sigma\cdot\frac{\cos(\theta)-\sin(\theta)}{a} \quad \overset{\theta=0}{\Longrightarrow} \quad \frac{2}{a}\,\sigma. \tag{3b}$$

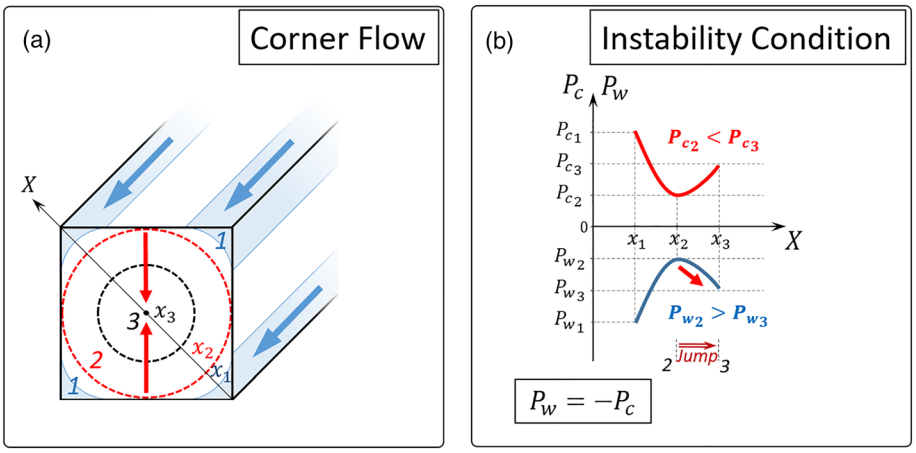

Figure 9. (a) Gas-water interface configurations at three subsequent times during swelling corner flow. Interface 1 is a stable interface, whereas Interface 2 (red dashed line) is an unstable interface. The interface jumps across the whole cross section to a stable meniscus across the duct, that is, to its end point 3. (b) Corresponding capillary- and water phase pressures. The water phase pressure (air gauge: $p_{air} = 0$) is at its maximum at Interface 2 and thermodynamical system will jump into the stable State 3 with lower water phase pressure. This Haines jump or snap-off is the basic mechanism of snap-off trapping.

The corresponding water phase pressures (air gauge: $p_{air} = 0$) are

$$p_{w,\,p} = -4\sigma \cdot \frac{\cos(\theta)}{a} \quad \overset{\theta=0}{\Longrightarrow} \quad -\frac{4}{a}\,\sigma \tag{4a}$$

and

$$p_{w,\,so} = -2\sigma \cdot \frac{\cos(\theta) - \sin(\theta)}{a} \quad \overset{\theta=0}{\Longrightarrow} \quad -\frac{2}{a}\,\sigma. \tag{4b}$$

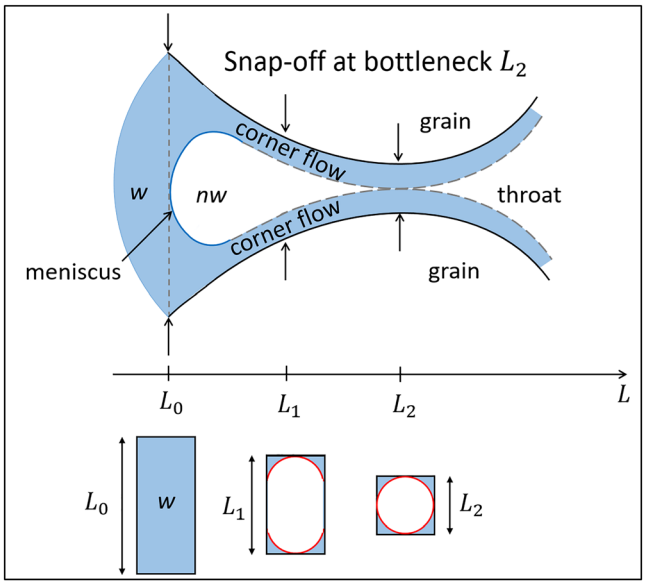

Figure 10. *Geometrical snap-off condition* for a concave-shaped pore channel (throat). (upper figure) Water phase (blue area, w = wetting phase, nw = nonwetting phase) distribution during CF. (lower figure) Fluid-fluid interface configurations (red lines) across the pore channel at different locations L. The interface at L_2 is unstable, because a further CF swelling leads to a smaller curvature and higher capillary pressure (lower water phase pressure, compare with Figure 9) and the interface will jump across the pore channel (Haines jump; snap-off).

For the special case $\theta = 0$ the three different temporal states during the swelling process of the corner flow are shown in Figure 9a) and indicated by 1, 2, 3. State 2 shows the unstable gas-water interface (red dashed line). Its curvature is $2/a$ and the snap-off capillary pressure is given by Equation 4b. The temporal course of the capillary pressure (red curve) and the water phase pressure (blue curve) is shown in Figure 9b). Physically, the air-water configuration is unstable, because any small perturbation will force the thermodynamical system to *jump* into the next stable State 3. Hence, the water meniscus will snap over the whole cross section and divide or split the defending gas phase.

The obvious problem is that such Haines jumps are not possible in a straight quadratic capillary, because water phase pressure for snap-off is always larger than for duct flow (Equation 4aand 4b); thus, duct flow will always occur before snap-off. This statement is also true for the general case of a rectangular duct (L&Z84). Therefore, snap-off trapping is unlikely to occur in pore networks with rectangular ducts.

For concave-shaped pore channels shown in Figure 10 the corresponding water phase pressure at the meniscus location L_0 and at the bottleneck of the pore channel L_2 are given by (L&Z84)

$$p_{w,\,p} = -2\sigma \cdot \left(\frac{1}{L_0} + \frac{1}{d}\right)\cos(\theta) \quad \overset{\theta=0}{\Longrightarrow} \quad -2\sigma\left(\frac{1}{L_0} + \frac{1}{d}\right) \tag{5a}$$

and

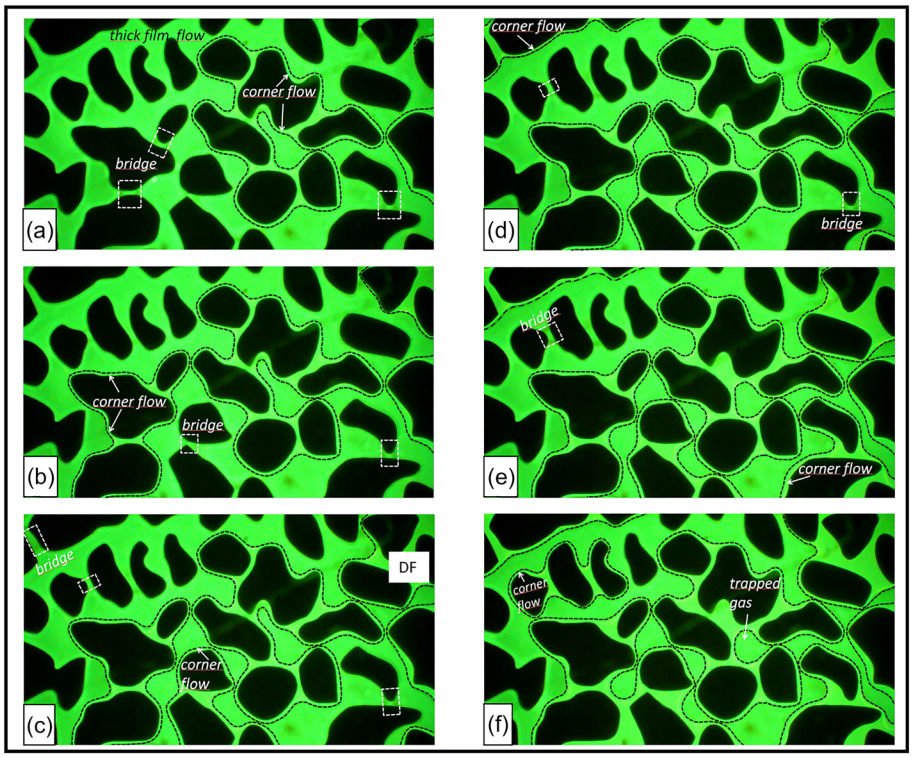

Figure 11. Snap-off trapping in MM4 glass ceramic micromodels at six subsequent times. (a) Precursor TFF leads to unstable bottleneck and water bridges occur (white dashed rectangles) and CF arises around closely adjacent grains (black dashed lines). This precursor CF has no connected path to the water saturated region shown in Figure 1. In the following time events it can be seen that snap-off occurs at the bridge locations, CF surrounds closely adjacent grains and trapped gas clusters occur (Image f) (Uranin tracer, fluorescence microscopy).

$$p_{w,so} = -2\sigma \cdot \frac{\cos(\theta) - \sin(\theta)}{L_2} \quad \overset{\theta=0}{\Longrightarrow} \quad -\frac{2}{L_2}\sigma, \tag{5b}$$

where d is depth of the pore channel. Hence, the *geometrical snap-off condition* for corner flow is given by

$$p_{w,so} \leq p_{w,p} \quad \overset{\theta=0}{\Longrightarrow} \quad L_2 \leq \frac{L_0 \cdot d}{L_0 + d}. \tag{6}$$

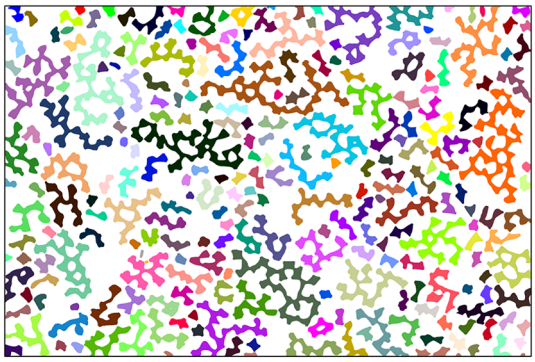

Figure 12. Trapped gas clusters within a representative window (34.5 mm × 23.5 mm) of the MM4 glass ceramic micromodel shown in Figure 3a). Seventy-three percent of the pore space is occupied with gas clusters. Grains and the water phase are not shown.

For our irregular micromodels MM4 L_0 is about 1 mm and the etching depth $d = 0.3$ mm. Snap-off will occur at all bottlenecks of the micromodel, where L_2 is smaller than 0.2 mm assuming a contact angle zero.

Figure 11 shows this complex trapping process within the 2-D sand analogs (glass ceramic micromodels) at six subsequent times at a capillary number 10^{-6}. At this capillary number CF occurs and the interplay of both flow types leads to a very efficient snap-off trapping mechanism. First, TFF covers the *whole* surface and provides enough water for water bridges at geometrical bottlenecks indicated by white dashed rectangles. If the *geometrical snap-off condition* is satisfied snap-offs (Haines jumps) occur at these bridge locations and CF develops around closely adjacent grains (black dashed lines). Note that this CF has *no connected path* to the water saturated region; it is fed by TFF alone. Further snap-off leads to trapped, ganglia-like gas clusters indicated (Figure 11f). The video of the snap-off trapping process is provided in the supporting information (Movie S2-MM4-Glass-TFF-CF-SO-trapping).

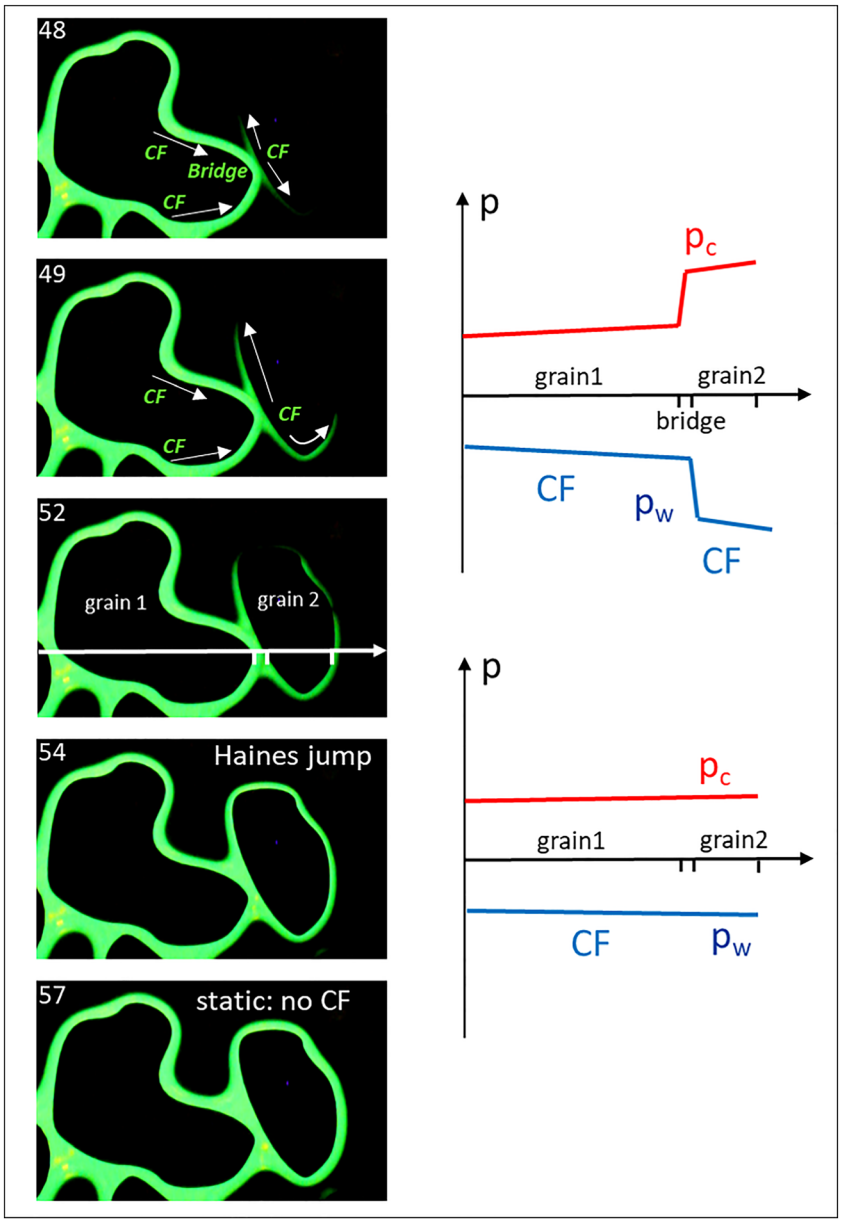

Figure 13. Precursor CF. (left) Time development of CF between unstable bridging (topmost image 48) and static water distribution (bottom image 57) in MM4-Si micromodels (Uranin tracer, fluorescence microscopy). (right) The capillary pressure (red curve) and the water phase pressure (left curve) are shown across the two adjacent grains (white arrow in Image 52). The drop of the water phase pressure indicates the unstable interface configuration at the bottleneck (water bridge). At this position snap-off occurs, then the pressure gradient weakens (Image 54) and balances itself out (Image 57).

Figure 12 shows the spatial distribution of trapped gas clusters of different sizes at breakthrough of DF at $Ca = 10^{-6}$. The mean residual gas saturation of the whole micromodel is 73%. We note that the cluster size distribution shows *universal scaling*.

4.2. Capillary Trapping in 2-D Micromodels With Smooth Surface

In this section we study the impact of *pore space structure* on the geometry of the displacement front and on trapping efficiency. We focus on the *geometrical snap-off condition* and suppress complete wetting. Therefore, we consider only micromodels with *smooth surfaces*, that is, we compare the trapping behavior of MM4-Si (irregular structure, 2-D sand analog, Figure 2a) with that of MM5-Si (stochastic lattice

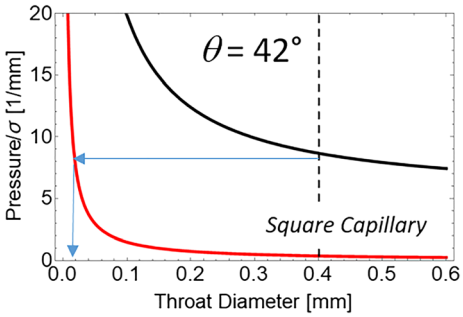

Figure 14. Comparison of piston flow (black) and snap-off (red) capillary pressure (Equations 3a and 3b) for a square capillary (400 μm × 400 μm) and the silicon contact angle $\theta = 42°$. The pressure is given in units of the interface tension σ.

structure, Figure 2b). Note that the averaged contact angle of Si micromodels is 42°. Based on this comparison we will discuss some experimental results in recent literature, which seem to contradict our main conclusions about the contact angle dependency of the trapping behavior.

MM4 Si micromodels, irregular pore space structure. The mean trapped gas saturation within the MM4-Si micromodel is 32%, that is, compared to the glass ceramic micromodel it is reduced by a factor 0.44. This strong decrease in trapping efficiency indicates a trapping transition, that is, the trapping process must have changed, qualitatively. The trapping process is now bypass trapping due to CF, because complete wetting and precursor TFF is not possible in MM4-Si micromodels (see Figure 13). Now the CF path is connected to the water-saturated region of DF. If the geometric snap-off condition is fulfilled then a water bridge at a bottleneck occurs (topmost image of Figure 13) with subsequent CF around the adjacent grain. The fractal CF front leads to CF-bypass trapping with a reduced trapping efficiency of about 50% compared to the *TFF*-snap-off trapping in the MM4-glass ceramic micromodel. We emphasize that both micromodels exhibit the same irregular *pore space structure* (2-D sand analogs). The qualitative difference between the two trapping mechanisms is only determined by the *surface roughness*. For the MM4-glass ceramic micromodel both trapping conditions are fulfilled, whereas for the MM4-Si micromodel the complete wetting condition is violated. This leads to a transition in trapping efficiency from 73% to 32% gas trapping. The video of corner flow bypass trapping process is shown in a video provided in the supporting information (video 3-MM4-Si-CF-BP-trapping). To the best of our knowledge such an experimental study of CF-bypass trapping mechanisms is lacking in current literature. We note that this trapping mechanism has to be distinguished from the well-known DF-bypass trapping.

MM5-Si micromodels, regular pore space structure. Figure 14 compares the piston flow capillary pressure (black curve, Equation 3a) with the snap-off capillary pressure (red curve, Equation 3b) of a square capillary for the contact angle of silicon. For a straight capillary with a width of 400 μm (mean channel width of the micromodel MM4, see Figures 15b and 15d) the piston flow pressure is always larger (Factor 20). For a pore space structure (topology), which possess narrow throats with a width of about 0.02 mm the snap-off pressure equals the piston flow pressure and snap-off becomes possible. Inspecting the pore size distribution of MM5-Si (Figure 15d), such small pores are not present. Therefore, snap-off is not possible, and the *geometrical trapping condition* is violated. This leads to flat front advance and *no* trapping for both MM5-micromodels (silicon and glass ceramic; MM5-Si: Figures 15b and 15f); MM5-glass ceramic is not shown). The flat front advance of DF is caused by interface smoothing and cooperative filling and is similar to that within GBS-monolayer discussed in part one of this study. The video is provided in the supporting information (Movie S4-MM5-Si-flat-front).

In contrast the *irregular pore space structure* of the micromodel MM4-Si (2-D sand analog) exhibits a lot of small throats as its pore size distribution shows (Figure 15c). Therefore, the geometrical trapping condition is satisfied and precursor CF leads to a fractal displacement front (Figure 15e) and to bypass trapping of about 30% of the pore space (Movie S3-MM4-Si-CF-BP-trapping).

Experimental and theoretical results for 2-D micromodels with smooth surface and ideal circular grains show *critical contact angles* θ_c in the range of 60–80° for low capillary numbers $Ca \approx 10^{-6}$: Cieplak and Robbins (1988): 60°; Jung et al. (2016): 80°; Hu et al. (2018): 60°; Wang et al. (2019, 2020): 60°. The *key question* is whether a *compact displacement front* and no trapping is observed, because $\theta_{Si} = 42° < \theta_c \approx 60°$. As shown above the answer depends on the *pore space structure* of the porous media. The MM5-Si micromodel shows a *compact displacement front* with no trapping, whereas the MM4-Si micromodel shows *fractal CF front* with trapping.

As an instructive example we analyzed the micromodel experiments conducted by Jung et al. (2016). They studied the displacement process in high-porosity (0.85) 2-D micromodels with ideal circular grains and *smooth* surface for *Ca* between 3×10^{-9} and 10^{-4}. To cover a contact angle range from 46° to 180° they used various combinations of fluids and wall materials. They found a transition between stable compact displacements with no trapping for $\theta < 80°$ to capillary fingering with trapping for $\theta > 120°$. Figure 1c in Jung

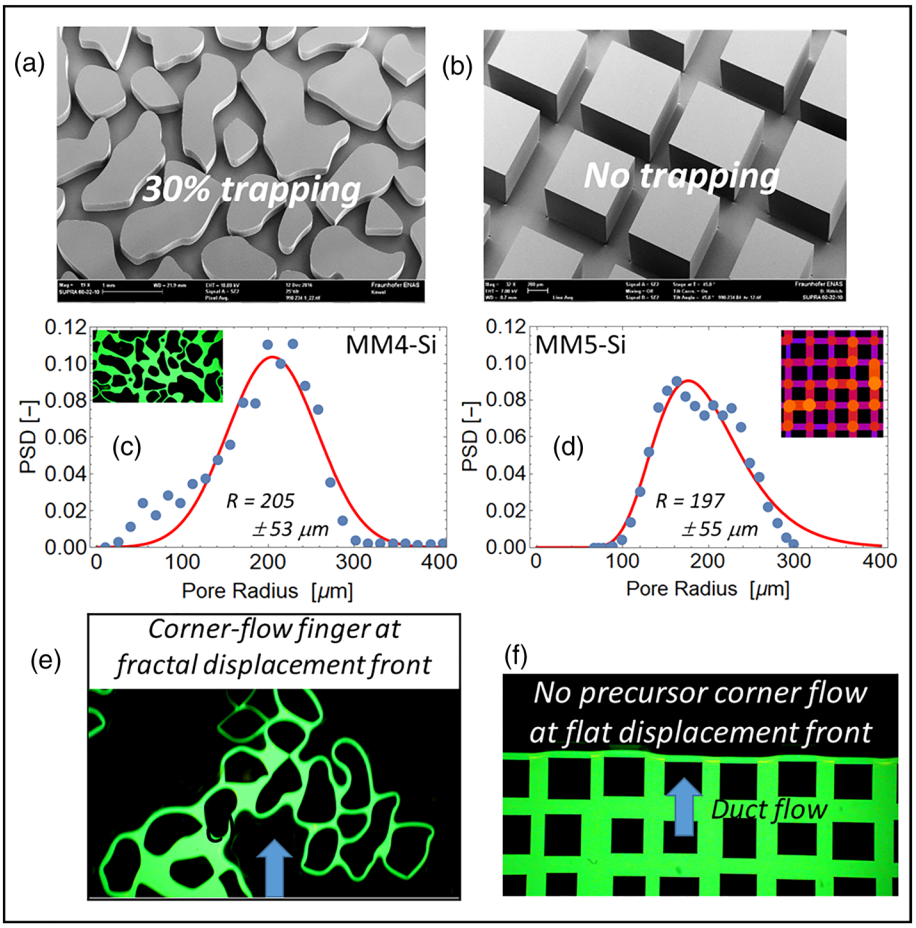

Figure 15. Impact of pore space structure (a, b) and frequency of small pores (=bottlenecks, c, d) on the geometry of the displacement front and on trapping efficiency (e, f) for MM4-Si and MM5-Si. The blue arrows in (e) and (f) indicate the direction of the invading water flow (Uranin tracer, fluorescence microscopy).

et al. (2016) shows the compact displacement front and the fluid saturations for three subsequent times. At breakthrough there is no trapped defending fluid. The contact angle of 46° corresponds rather well to the silicon contact angle of 42°.

Our counter example MM4-Si shows that depending on the pore space structure a fractal displacement front is possible. Hence, this *smoothing effect* that is intensively discussed and studied experimentally and numerically in literature (see references in Geistlinger & Zulfiqar, 2020) is connected to *artificial* porous media, which exhibit a *smooth* surface, a *high porosity* (0.6–0.85), and *ideal circular* grains.

5. Conclusions

We studied the impact of pore space structure (*morphology* and *connectivity* of the pore space) and the physicochemical surface properties (*wettability* and *roughness* of the pore-solid interface) on capillary trapping in 2-D and 3-D porous media. We used sand packs as the 3-D porous media and micromodels with different pore space structures and surface roughness as the 2-D porous media. We developed a new 3-D-2-D mapping algorithm to represent important morphological properties of the 1 mm sand pack. The *Simulating-Annealing* algorithm maps the porosity and the chord length distributions of the sand pack to the 2-D microstructure (MM4, 2-D sand analogs). We also used micromodels with a stochastic lattice structure to study the impact of pore space structure on displacement and trapping. To represent the *rough surface* of natural sands the micromodels were produced from a glass ceramic. All microstructures were produced by glass ceramic and silicon (*smooth surface*), in order to study the impact of surface roughness. The glass ceramic micromodels were constructed using an *anisotropic* photolithographic etching process based on the photosensitive

glass ceramic FOTURAN. For the production of the Si-micromodels an interval-based ICP-DRIE-technology was applied for *anisotropic* etching.

Our main conclusion is that capillary trapping in porous media depends on two necessary conditions, the *complete wetting* condition and the *geometrical snap-off* condition:

i. If both conditions are satisfied the highly efficient snap-off trapping mechanism is possible, which is caused by precursor thick-film flow (experimental proof: trapping in natural sands and micromodels MM4-glass ceramic with rough surfaces).
ii. If the complete wetting conditions is not satisfied the trapping behavior changes qualitatively from snap-off trapping to bypass trapping. The trapping efficiency is reduced by approximately 50% (experimental proof: increasing the contact angle in sand packs from 5° to 115°; comparing micromodels with irregular pore space structure and different degree of surface roughness).
iii. If the *geometrical snap-off condition* is not satisfied trapping is *not* possible. This shows the strong impact of pore space structure (frequency of small throats/bottlenecks) on trapping (experimental proof: comparing silicon micromodels (smooth surfaces) with different pore space structure (irregular and lattice structure, which have approximately the same porosity and the same mean pore diameter).

Sand and glass beads show a completely different and *opposite* functional contact angle dependency. *Glass bead packs* show a crossover from no-trapping to maximal trapping with an increase in the contact angle. Conversely, *sand packs* show inverse nonmonotonous behavior; that is, at low contact angles (5–33°) maximal trapping occurs, followed by a crossover to no trapping (81–88°) and then medium trapping (99–115°). Since both porous media exhibit similar morphological properties (similar Minkowski functions: porosity, surface density, mean curvature density, Euler number density, Geistlinger et al., 2015), we deduce that this difference in behavior is caused by the difference in surface roughness that allows complete wetting and hence precursor TFF for natural sand. Consequently, the *smoothing effect* that leads to this sharp transition in glass bead packs (as has been intensively studied in recent literature) is only relevant in *artificial* porous media (i.e., those which have a smooth surface, high-porosity, and circular grains).

Data Availability Statement

The data can be accessed at this site (https://www.ufz.de/index.php?en=39791).

Acknowledgments
This work was supported by the BMBF (TESTUM project, FKZ 03A0017C) and the DFG (GE 766/12–1). We thank the technician Bernd Apelt for technical help and Steffen Schlueter for providing the Simulated Annealing algorithm for 3-D-2-D mapping.

References

Adler, P. M., & Brenner, H. (1988). Multiphase flow in porous media. *Annual Review of Fluid Mechanics*, *20*(1), 35–59. https://doi.org/10.1146/annurev.fl.20.010188.000343

AlRatrout, A., Blunt, M. J., & Bijeljic, B. (2018). Wettability in complex porous materials, the mixed-wet state, and its relationship to surface roughness. *Proceedings of the National Academy of Sciences of the United States of America*, *2018*(115), 8901–8906. https://doi.org/10.1073/pnas.1803734115

Bico, J., Tordeux, C., & Quéré, D. (2001). Rough wetting. *Europhysics Letters*, *55*(2), 214–220. https://doi.org/10.1209/epl/i2001-00402-x

Blunt, M. J. (2017). *Multiphase Flow in Permeable Media: A Pore-Scale Perspective*. Cambridge: University Press. https://doi.org/10.1017/9781316145098

Brücher, M., & Bottlinger, M. (2006). Dreidimensionale Computersimulation zur Untersuchung von Partikelschüttungen aus unregelmäßig geformten Partikeln. *Chemie Ingenieur Technik*, *78*(6), 727–733. https://doi.org/10.1002/cite.200500185

Cazabat, A. M., & Stuart, M. A. C. (1986). Dynamics of wetting: Effects of surface roughness. *The Journal of Physical Chemistry*, *90*(22), 5845–5849. https://doi.org/10.1021/j100280a075

Cieplak, M., & Robbins, M. O. (1988). Dynamical transition in quasistatic fluid invasion in porous media. *Physical Review Letters*, *60*(20), 2042–2045. https://doi.org/10.1103/PhysRevLett.60.2042

de Gennes, P. G. (1985). Wetting: Statics and dynamics. *Reviews of Modern Physics*, *57*(3), 827–863. https://doi.org/10.1103/RevModPhys.57.827

Dullien, F. A. L. (1992). *Porous Media: Fluid Transport and Pore Structure* (2nd ed., Vol. 48, p. 372). San Diego, CA: Academic. https://doi.org/10.1016/0375-6742(93)90016-F

Geistlinger, H., Ataei-Dadavi, I., Mohammadian, S., & Vogel, H. J. (2015). The impact of pore structure and surface roughness on capillary trapping for 2-D and 3-D porous media: Comparison with percolation theory. *Water Resources Research*, *51*, 9094–9111. https://doi.org/10.1002/2015WR017852

Geistlinger, H., Ding, Y., Apelt, B., Schlueter, S., Küchler, M., Reuter, D., et al. (2019). Evaporation study based on micromodel experiments: Comparison of theory and experiment. *Water Resources Research*, *55*, 6653–6672. https://doi.org/10.1029/2018WR024647

Geistlinger, H., Krauss, G., Lazik, D., & Luckner, L. (2006). Direct gas injection into saturated glass beads: Transition from incoherent to coherent gas flow pattern. *Water Resources Research*, *42*, W07403. https://doi.org/10.1029/2005WR004451

Geistlinger, H., & Zulfiqar, B. (2020). The impact of wettability and surface roughness on fluid displacement and capillary trapping in 2D- and 3D-porous media. Part 1: Wettability-controlled phase transition of trapping efficiency in glass beads packs. *Water Resources Research*, *56*, e2019WR026826. https://doi.org/10.1029/2019WR026826

Hu, R., Wan, J., Kim, Y., & Tokunaga, T. K. (2017). Wettability impact on supercritical CO_2 capillary trapping: Pore-scale visualization and quantification. *Water Resources Research*, *53*, 6377–6394. https://doi.org/10.1002/2017WR020721

Hu, R., Wan, J., Yang, Z., Chen, Y.-F., & Tokunaga, T. K. (2018). Wettability and flow rate impacts on immiscible displacement: A theoretical model. *Geophysical Research Letters*, *45*, 3077–3086. https://doi.org/10.1002/2017GL076600

ISO-standard: International Organization for Standardization. (1997). Geometrical product specifications (GPS)—Surface texture: Profile method—Terms, definitions and surface texture parameters (ISO Standard No 4287). Retrieved from https://www.iso.org/standard/10132.html

Johnson, R. E., & Dettre, R. H. (1964). In R. F. Gould (Ed.), *Contact angle, wettability, and adhesion*. Washington, DC: American Chemical Society. https://doi.org/10.1021/ba-1964-0043.ch007

Jung, M., Brinkmann, M., Seemann, R., Hiller, T., Sanchez de La Lama, M., & Herminghaus, S. (2016). Wettability controls slow immiscible displacement through local interfacial instabilities. *Physical Review Fluids*, *1*(7), 074202. https://doi.org/10.1103/PhysRevFluids.1.074202

Kibbey, T. C. G. (2013). The configuration of water on rough natural surfaces: Implications for understanding air-water interfacial area, film thickness, and imaging resolution. *Water Resources Research*, *49*, 4765–4774. https://doi.org/10.1002/wrcr.20383

Kuechler, M., Otto, T., Gessner, T., Ebling, F., & Schroeder, H. (2003). Hot embossing for MEMS using silicon tools. *International Journal of Computer Engineering and Science*, *04*(03), 609–612. https://doi.org/10.1142/S1465876303001873

Lenormand, R., Touboul, E., & Zarcone, C. (1988). Numerical models and experiments on immiscible displacement in porous media. *Journal of Fluid Mechanics*, *189*, 165–187. https://doi.org/10.1017/S0022112088000953

Lenormand, R., & Zarcone, C. (1984). *Role of Roughness and Edges during Imbibition in Square Capillaries*. Houston, Texas: Society of Petroleum Engineers. https://doi.org/10.2118/13264-MS

Mehmani, A., Kelly, S., Torres-Verdín, C., & Balhoff, M. (2019). Residual oil saturation following gas injection in sandstones: Microfluidic quantification of the impact of pore-scale surface roughness. *Fuel*, *251*, 147–161. https://doi.org/10.1016/j.fuel.2019.02.118

Netz, R. R., & Andelman, D. (1997). Roughness-induced wetting. *Physical Review E*, *55*(1), 687–700. https://doi.org/10.1103/PhysRevE.55.687

Schlueter, S., Weller, U., & Vogel, H. J. (2010). Segementation of X-ray microtomography images of soil using gradient masks. *Computers & Geosciences*, *36*, 1246–1251. https://doi.org/10.1016/j.cageo.2010.02.007

Shibuichi, S., Onda, T., Satoh, N., & Tsujii, K. (1996). Super water-repellent surfaces resulting from fractal structure. *The Journal of Physical Chemistry*, *100*(50), 19,512–19,517. https://doi.org/10.1021/jp9616728

Voburger, T. V., & Raja, J. (1990). *Surface finish metrology tutorial (NISTIR 89–4088)*. Gaithersburg, MD: US Department of Commerce, National Institute of Standards and Technology.

Wang, Z., Chauhan, K., Pereira, J.-M., & Gan, Y. (2019). Disorder characterization of porous media and its effect on fluid displacement instabilities. *Physical Review Fluids*, *4*, 074202. https://doi.org/10.1103/PhysRevFluids.4.034305

Wang, Z., Pereira, J.-M., & Gan, Y. (2020). Effect of wetting transition during multiphase displacement in porous media. *Langmuir*, *36*, 2449–2458. https://dx.doi.org/10.1021/asc.langmuir.9b03780

Wenzel, R. N. (1936). Resistance of solid surfaces to wetting by water. *Industrial and Engineering Chemistry Research*, *28*(8), 988–994. https://doi.org/10.1021/ie50320a024

Wilkinson, D. (1984). Percolation model of immiscible displacement in the presence of buoyancy forces. *Physical Review A*, *30*(1), 520–531. https://doi.org/10.1103/PhysRevA.30.520

Zhao, B., MacMinn, C. W., & Juanes, R. (2016). Wettability control on multiphase flow in patterned microfluidics. *Proceedings of the National Academy of Sciences of the United States of America*, *113*(37), 10,251–10,256. https://doi.org/10.1073/pnas.1603387113

Zue, L., Zhang, C., Falta, R. W., & Benson, S. M. (2013). Micromodel investigations of CO_2 exsolution from carbonated water in sedimentary rocks. *Advances in Water Resources*, *53*, 188–197. https://doi.org/10.1016/j.advwatres.2012.11.004